Tailoring resisitivity anisotropy of nanorippled metal films: Electrons surfing on gold waves

Daniele Chiappe,* Andrea Toma,† and Francesco Buatier de Mongeot‡
Dipartimento di Fisica–Università di Genova and CNISM, Via Dodecaneso 33, 16146 Genova, Italy
(Received 23 February 2012; published 9 July 2012)

By using self-organized patterning of polycrystalline Au electrodes, we demonstrate that the electrical resistivity of the film can be forced to become strongly anisotropic by tailoring a nanoscale ripple undulation at the metal-vacuum interface. Electrons traveling orthogonally to the nanoripples are affected by a strong increase in resistivity, while when electrons travel parallel to the undulations of the rippled film, the resistivity is almost unaffected and even shows a slight reduction. The observations are quantitatively interpreted within the semiclassical size-effect regime in terms of an increase of surface scattering from the large-scale corrugations and of a reduction of diffuse scattering from atomic-scale roughness.

DOI: 10.1103/PhysRevB.86.045414 PACS number(s): 73.61.Ga, 81.65.Cf, 79.20.Rf

I. INTRODUCTION

A fine control of the mechanisms which characterize the conductive behavior of thin films and metallic interconnect lines is crucial for optimally tailoring the electronic performance of integrated circuits and devices. In fact, due to substantial technological progress in controlled nanofabrication techniques, the electronics industry has rapidly scaled down the dimensions of the interconnects towards the 10-nm range. Under these conditions, power dissipation due to Ohmic losses in the metal contacts is becoming one of the limiting factors which hinder further integration of the devices. This is due to the fact that, when one or more of the dimensions characterizing a conductor, e.g., film thickness or the width of a metallic interconnect line, become comparable to the mean-free path ξ of the charge carriers, typically in the 30–40 nm range for noble metals, an additional term must be added to the expression of the resistivity in order to take into account electron scattering at the rough metal-vacuum interface in the so called "size-effect" regime.[1–4] In a conventional growth experiment, both grain size and film roughness scale with film thickness, thus making it difficult to disentangle their contribution to the electrical resitivity.[4–6] In this context, we have investigated the possibility of tailoring the anisotropy of electrical conductivity in an otherwise isotropic thin metal film by modifying its *morphology* at the vacuum interface while keeping constant the distribution of polycrystalline grains. For this purpose, we employed a self-organized process based on ion beam sputtering, probing *in situ* and in real time the resistivity of the Au metal films during the formation and amplification of a nanoscale ripple pattern, until the film decomposed into a partially disconnected nanowire array.

The pictorial description provided in the title represents well the intriguing conclusions: while the electrical resistivity measured orthogonal to the wave ridges increases by orders of magnitude when the amplitude of the undulations grows, counterintuitively, the resistivity measured parallel to the surface undulations shows a small but evident decrease even if the film thickness is reduced well into the size-effect regime.

Surface nanostructuring has been performed using a bottom-up approach based on defocused ion beam sputtering (IBS).[7,8] Self-organized pattern formation is a consequence of morphological rearrangement of the surface once destabilized by the ion beam: the competition between mass diffusion mechanisms and the erosive action of the ion beam determines the evolution of nanoscale ripple structures with controllable orientation depending on the sputtering geometry. Recent investigations have demonstrated the possibility to extend IBS to pattern the surface of polycrystalline metal films irradiated at glancing angles.[9–12] This specific geometrical condition promotes the formation of elongated ripples which propagate for several microns across the grain boundaries, a process which is driven by the shadowing action of the initial surface roughness.[10,11] The amplitude of the ripple modulation and its lateral periodicity evolve as a function of the ion dose, thus making it possible to modify the pattern morphology by controlling the exposure time to the ion source. It is important to notice that, due to the erosive action of the ion beam, the metal film is progressively consumed until the bottom of the ripple valleys reaches the substrate.[13,14] In the final stage of the experiment, the film decomposes into a partially connected array of polycrystalline nanowires.

II. EXPERIMENTAL SECTION

Polycrystalline Au (Goodfellow, purity 99.99%) metal films were thermally deposited on soda-lime glass substrates at a rate of 6 nm/min by means of a resistively heated tungsten/alumina crucible. A calibrated quartz-crystal microbalance was used for monitoring the total thickness. Deposition was accomplished at room temperature within a custom designed vacuum system with a base pressure in the low 10^{-7} mbar range.

Irradiation with a defocused Ar^+ ion beam (5N purity) was performed *in situ* using a gridded multiaperture ion source (Tectra Instruments). The patterning [see the sketch in Fig. 1(a)] was done at an off-normal sputtering angle $\theta = 82^\circ$ (measured with respect to the surface normal) and ion energy $E = 800$ eV. A biased tungsten filament providing electrons via thermionic emission was placed close to the extraction grid in order to compensate surface charging effects due to ion implantation into the dielectric substrate. The total current (ions plus electrons) captured by the gold electrode at 82° was thus minimized in the range below 1 μA during ion irradiation. The sample holder temperature was controlled around $T = 230$ K during the sputtering process by means of a liquid-nitrogen cooling system in order to prevent excessive surface heating. Under such conditions, the surface temperature (as determined

 ©2012 American Physical Society

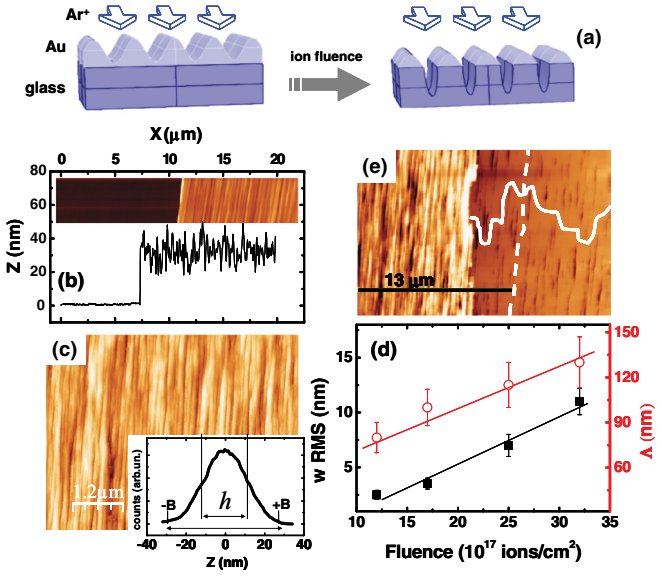

FIG. 1. (Color online) (a) Schematic representation of the ion beam nanostructuring process. (b) (Top) AFM topography of the Au film after irradiation to an ion fluence $\Theta = 25 \times 10^{17}$ ions/cm^2 ($d_0 = 150$ nm). The left portion of the image represents the glass substrate exposed by a mechanical scratch. (Bottom) AFM line profile along the scratched topography. (c) High-resolution AFM image of a sputtered Au film exposed to an ion fluence $\Theta = 35 \times 10^{17}$ ions/cm^2. Inset: histogram representing the height distribution. (d) Surface rms roughness and ripple wavelength as a function of ion fluence; the experimental data are interpolated by a linear best fit. (e) AFM topography after a mechanical scratch of the Au film shown in panel (c); the scratched portion of the sample on the right evidences the formation of elongated grooves, which propagate into the glass surface in correspondence of the metal film disconnection. The solid line and the dotted line schematically represent electronic motion along the transverse and longitudinal directions.

by means of an infrared pyrometer) was stabilized around 310 K. In order to monitor the erosion process *in situ* and in real time, we analyzed the atoms ejected from the sputtered surfaces using secondary neutral mass spectrometry (SNMS).

Four-wire resistance measurements were performed in real time during the sputtering process using two digital multimeters (HP 3478A) coupled to a Lab-view data acquisition tool. The multimeters, operating in the range 0–100 Ω, provide a current of 100 μA. We verified that the net current deriving from the external ion/electron sources does not alter the resistance measurement with accuracy in the 1% range. The two gold square electrodes, deposited by the aforementioned procedures, were wired in such a manner to measure the sheet resistance respectively along the beam direction and orthogonally to it as sketched in Fig. 2(c).

The morphologies of the patterned gold films have been analyzed *ex situ* by means of an atomic force microscope (AFM Nanosurf Mobile S) equipped with ultrasharp Si probes (PPP-NCLR, Nanosensor) operated in intermittent contact mode. In order to achieve a direct evaluation of the thickness of the residual metal film, we have investigated by AFM portions of surfaces where the film was mechanically scratched using a micrometric tip. In such a manner, we were able to acquire in the same AFM topography both the residual gold film and the

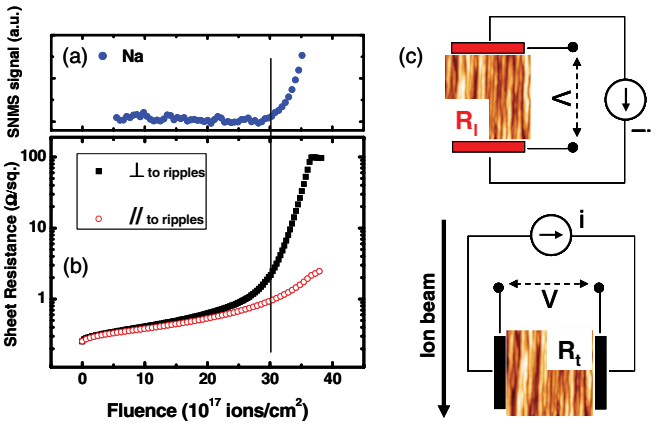

FIG. 2. (Color online) (a) Real-time evolution of the SNMS signal originating from Na atoms emitted by the glass substrate after the rupture of the Au film; the onset of the metal film disconnection is located at the fluence $\Theta \approx 30 \times 10^{17}$ ions/cm^2 (vertical solid line). (b) Real-time evolution of the sheet resistances measured during sputtering, respectively, along parallel (red open circles) and orthogonal (black squares) directions with respect to the ripples. For the sake of clarity, approximately only one data point every 100 has been plotted. (c) Sketch of the four-wire sheet resistance measurements scheme employed in (b).

underling glass substrate to determine the level of the interface and to visualize the grooves.

III. RESULTS

Au films on glass substrates were sputtered at glancing angles, as sketched in Fig. 1(a). As shown in Fig. 1(b) and in agreement with the results described by Toma *et al.*,[9,10] after a polycrystalline gold film with initial thickness $d = 150$ nm is irradiated by Ar^+ ions up to a fluence $\Theta = 25 \times 10^{17}$ ions/cm^2, one can observe a regular pattern made up of connected ripples elongated along the beam projection. The residual gold film presents an average thickness d around 30 nm, as revealed by the line scan across a mechanical scratch [inset in Fig. 1(b)]. From higher-resolution AFM images [an example is shown in Fig. 1(c)], we determine the rms roughness which in this case amounts to $\sigma_{rms} = 7$ nm (the corresponding average peak-to-valley amplitude h for a sinusoidal profile, given by the relation $h = 2\sqrt{2}\sigma_{rms}$, in this case reads 19 nm) and the average wavelength $\Lambda \approx 120$ nm. In Fig. 1(d), we plot the average wavelength Λ of the Au ripple pattern and the surface rms roughness σ_{rms} as a function of increasing ion fluence: to a first approximation, both the roughness and the wavelength evolve following a linear trend with values respectively in the range of 10 and 100 nm. By increasing further ion fluence [$\Theta = 35 \times 10^{17}$ ions/cm^2, Fig. 1(e)], the deeper ripple valleys reach the glass substrate and the gold film begins to disconnect. Consequently, elongated grooves propagate into the glass substrate [right portion of Fig. 1(e)] due to the ion etching process, as sketched in Fig. 1(a). The corresponding SNMS measure, which was acquired during the erosion process, is reported in Fig. 2(a): the fast increase of the Na signal (one of the glass substrate components) identifies the onset of nanowire disconnection at fluence $\Theta \approx (30 \pm 1) \times 10^{17}$ ions/cm^2. The minimum

area of the glass surface (detection limit), which needs to be exposed in order to produce a measurable SNMS signal, was estimated around 2% of the total. The sheet resistances R_L and R_T measured following the procedure described in the experimental section are shown in Figs. 2(b) and 2(c): for increasing ion fluence (decreasing film thickness), two markedly different trends can be observed, thus evidencing the appearance of a clear conduction anisotropy induced by ion sputtering. This anisotropy is strongly amplified when the Au nanowires begin to locally disconnect; in particular, electric conduction is favored along the longitudinal direction, with sheet resistance values in the 1 Ω/sq. range, while the transverse resistance R_T shows a fast increase towards the 100 Ω/sq. range. The latter value was arbitrarily chosen as the common end point of these experiments; indeed, by further increasing ion fluence, the transverse resistance R_T would continue to grow sharply (notice the log scale of the graph) until electrical continuity is lost.

In the following, our attention will be mainly focused on the intriguing behavior of electrical conduction well before the onset of nanowire disconnection, indicated by the increase of the Na signal in Fig. 2(a) ($\Theta \approx 30 \times 10^{17}$ ions/cm^2). The trends of the sheet resistances in fact show clear evidence of an anisotropic behavior which can not be attributed to percolative conduction mechanisms since the gold film is still completely connected [see Fig. 1(a)]. The observation of resistance anisotropy *before* nanowire disconnection, i.e., in absence of percolation, is due to the increasing importance of surface scattering in the size-effect regime, when the film thickness becomes comparable with the mean-free path of electrons in a gold bulk ($\xi \approx 37$ nm around room temperature).[6] In this case, anisotropic surface scattering from the one-dimensional surface modulations determines the increase of the transverse resistivity for electrons traveling orthogonally to the Au nanowaves. Only after the ripple pattern decomposes into disconnected nanowires does percolative charge transport become the dominant process, with conduction taking place along the transverse direction [as sketched by the solid white line in Fig. 1(d)]. The importance of percolation becomes less relevant when conduction takes place along the ripple axis since the nanowires tend to bifurcate, forming an interconnected elongated network [as sketched by the dashed white line in Fig. 1(d)].

In order to investigate the correlation between surface morphology and anisotropic resistivity, the same experiment was replicated employing Au films with increasing initial thickness: higher ion doses are required to consume the gold film and the pattern evolution is consequently further protracted. In such a manner, higher and wider Au ripple corrugations can be obtained in correspondence to equivalent values of the residual film thickness. The initial thickness values were chosen to be $d_0^a = 80$ nm, $d_0^b = 150$ nm, $d_0^c = 300$ nm (where indexes a, b, c identify the samples). In Fig. 3(a), we plot the evolution of the parallel (R_L) and transverse (R_T) sheet resistances as a function of ion fluence for the three samples (a, b, c). For the sake of clarity, approximately only one data point every 100 has been plotted, but all data points have been used in the fits discussed in the following. As expected for an isotropic film, R_T and R_L have a common starting value which scales with the initial film thickness d_0 since the sheet resistance is

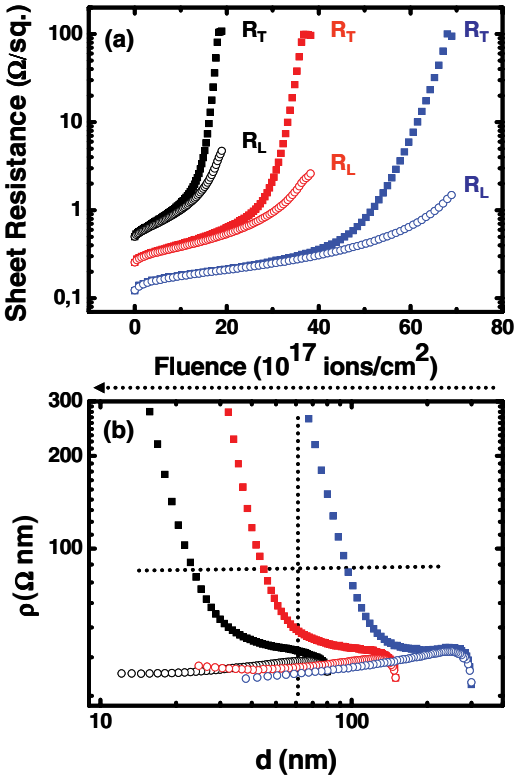

FIG. 3. (Color online) (a) Evolution of sheet resistances as a function of ion fluence for the sputtered sample a (black traces, initial thickness $d_0 = 80$ nm), sample b (red traces, initial thickness $d_0 = 150$ nm), and sample c (green traces, initial thickness $d_0 = 300$ nm). The open circles describe the evolution of the longitudinal resistances R_L, while filled squares correspond to the transverse resistances R_T. (b) Evolution of resistivity obtained from the data of panel (a); the ion fluence is now converted into residual Au thickness. The black dotted line corresponds to a vertical cut at the thickness $d = 60$ nm. For the sake of clarity, approximately only one data point every 100 has been plotted.

defined as $R = \rho/d$. For samples with a higher initial thickness d_0, increased ion doses are required before the end-point value $R_T = 100$ Ω/sq. of the transverse sheet resistance is reached. As shown in Fig. 3(a), at the fixed common end values of $R_T = 100$ Ω/sq., longitudinal conduction appears to be favored for the initially thicker films; the values of R_L scale down from the end value of 4 Ω/sq. (sample a, $d_0^a = 80$ nm), to $R_l \approx 2$ Ω/sq. (sample b, $d_0^b = 150$ nm) reaching $R_l \approx 1.3$ Ω/sq. (sample c, $d_0^c = 300$ nm). The resistance anisotropy R_T/R_L can consequently be amplified by simply increasing the amplitude of the ripple undulations, i.e., by scaling up the initial thickness of the gold film. The sheet resistances [Fig. 3(a)] can be converted into resistivity values, according to the relation $\rho = R \times d$. For this purpose, ion fluence (proportional to the irradiation time t) was converted into a residual film thickness $d(t)$ after having determined the effective erosion rate $\alpha = 1{,}20 \pm 0{,}10$ nm/min using AFM analysis of scratched gold films at different sputtering times [similar to Fig. 1(a)]. In Fig. 3(b), the resistivity trends ρ_L and ρ_T are reported as a function of the thickness for samples a, b, and c. At the initial temperature of 240 K, before starting sputtering, the resistivity values for the three samples are in

the range $\rho_0 = 35-40\ \Omega\cdot$nm. During the early stages of the sputtering process, a fast increase of the resistivity is observed: this transition extends for about 1300 s (corresponding to the removal of about 30 nm of Au). Such a transient is due to the temperature increase of the film under irradiation (as revealed *in situ* by means of IR pyrometry, data not shown). The temperature increase was measured to be around 70–80 K, a figure which is compatible with a 20% resistance increase, assuming the relation $(R-R_0)/R_0 = b(T-T_0)$ where $b = 3.4\times10^{-3}\ \mathrm{K}^{-1}$ is the resistance temperature coefficient for Au. After the initial transient, the resistivity values for samples *a*, *b*, and *c* saturate around 50 Ω nm.

In Fig. 3(b), one can notice that the transverse resistivity shows a remarkable enhancement, by more than one order of magnitude, as a function of increasing ion dose while the longitudinal resistivity does not show the same tendency, thus giving rise to the strong conduction anisotropy. It is worth noticing that, for equivalent values of the residual thickness, the sputtered metal films differ dramatically from each other in terms of their transverse resistivity ρ_T, while the variation of ρ_L is negligible. For example, a vertical cut through the plot in Fig. 3(b) at $d = 60$ nm (vertical dotted line) shows that the transverse resistivity ρ_T varies from $\rho \approx 55\ \Omega$ nm for sample *a*, with initial thickness $d_0^a = 80$ nm, to $\rho \approx 500\ \Omega$ nm for sample *c* with initial thickness $d_0^c = 300$ nm. This result is remarkable in its simplicity and it implies that by just changing the initial thickness of the film, one can control the resistivity anisotropy at a fixed residual coverage, in response to the different anisotropic morphology of the metal-vacuum interface. Although the variation of ρ_L is very small compared to the remarkable increment of ρ_T, in Fig. 3(b) (bottom traces) we can notice a trend which is common to all the samples: surprisingly, the longitudinal resistivity ρ_L presents a weak but clear decreasing trend when the film thickness is reduced. Based on simple considerations derived from the classical size-effect theory,[1–3] one would expect that the resistivity should increase when the film thickness is reduced in the range of the electron mean-free path or, in a limit condition, should stay constant for a flat film if electron scattering at the metal-vacuum interface were perfectly specular. We will come back to the interpretation of this weak but counterintuitive effect after discussing quantitatively the physical origin of predominant changes in the transverse resistivity [upper traces in Fig. 3(b)].

In the case of sample *c*, with $d_0^c = 300$ nm, the transverse resistivity ρ_T remains almost constant after the initial thermal transient, until the residual thickness is reduced in the range $d^* \approx 150$ nm. Below this value, the surface contribution to the resistivity becomes relevant and, consequently, ρ_T starts to evolve toward higher values (several hundreds of Ω nm) while the longitudinal resistivity ρ_L remains in the 50 Ω nm range. In agreement with the above observation, for samples *a* and *b*, whose initial thickness satisfy the condition $d_0 < d^*$ from the beginning, an increase of the transverse resistivity is immediately observed after the sputtering process is initiated.

IV. DISCUSSION

We tried to interpret the trends of resistivity versus residual thickness d on the basis of the analytical models here briefly introduced. According to Mathiessen's rule, a simplified form of the Fuchs-Sondheimer (FS) model describes the resistivity of a metal film as the sum of contributions from the bulk (ρ_0) and from the surface.[2,3] The latter assumes the form

$$\rho_{\mathrm{FS}} \approx \rho_0 + \rho_0 \frac{3}{8}(1-p)\frac{\xi}{d} = \rho_0 + \rho_0 \frac{C}{d}, \tag{1}$$

where ξ is the electron mean-free path in the bulk (a function of temperature, of the density of impurities, and of grain boundaries), d is the average thickness of the film, and p is the specularity parameter, which varies from 1 for fully specular scattering to 0 for fully diffuse scattering. For $p = 1$, during a scattering process the component of the electron momentum parallel to the surface is conserved and the orthogonal one is reversed, while for $p = 0$ the direction of the momentum is completely randomized. The parameter $C = 3/8\,(1-p)\,\xi$ thus assumes the physical meaning of an effective electron mean-free path taking into account surface scattering. This model, however, contains a strongly disputable premise since it assumes that the roughness is limited to corrugations of atomic-scale amplitude. When the amplitude of the surface corrugation abundantly exceeds the Fermi wavelength λ_F (for Au $\lambda_F \approx 0.5$nm), a model based on atomic-scale roughness is no longer adequate because additional morphological effects have to be taken into account. Finzel and Wiessmann[15] (FW) have theoretically extended the FS model in the limit of surface corrugations whose vertical excursion B is bigger than the Fermi wavelength, but significantly smaller than the film thickness ($\lambda_F \ll B \ll d$). The latter case applies to the present experiment for which the height distribution, derived from the AFM images [see, e.g., inset of Fig. 1(c)] adopts a quasi-Gaussian distribution with semi-amplitude B roughly amounting to $3\times\sigma_{\mathrm{rms}}$.

The relation describing the total resistivity thus becomes

$$\rho = \rho_0 + \frac{C}{d}\rho_0 + \frac{C\cdot B^2(d)}{d^3}\rho_0. \tag{2}$$

In our case, in particular at the later stages of sputtering, when a strong enhancement of ρ_T is observed, the ripple corrugations evolve towards a limit of vertical amplitudes comparable with the residual film thickness ($B \leqslant d$). As a consequence, it is evident that a description based on a "small" -scale roughness (FW model $B \ll d$) is expected to be insufficient to interpolate the experimental data, so that the contribution of large-scale ($B \approx d$) thickness fluctuations must be taken into account. A model based on these assumptions has been developed by Namba *et al.* [16] and, later, an analytical simplified formula for the total resistivity was derived by Prater in the ideal case of a sinusoidal surface profile with peak-to-valley amplitude h (Namba-Prater, NP model):[17]

$$\rho = \rho_0\left\{\left[1-\left(\frac{h}{d}\right)^2\right]^{-1/2} + \frac{C}{d}\left[1-\left(\frac{h}{d}\right)^2\right]^{-3/2}\right\}. \tag{3}$$

In order to compare the NP model, which assumes a pure sinusoidal profile, with our experimental results, the quantity h in Eq. (3) has been substituted with the function $h(t)S$, where $h(t) = 2\sqrt{2}\sigma_{\mathrm{rms}}$ is the average peak-to-valley ripple amplitude (derived from the AFM patterns) whose evolution with ion dose has been previously determined in Fig. 1(d), and S is a corrective factor which takes into account the overall height excursion $2B$ of the topography. For a morphology endowed

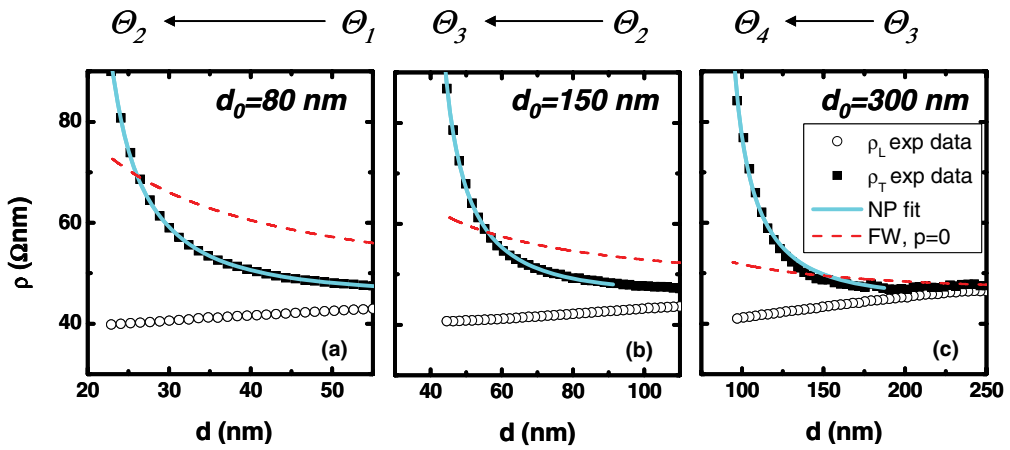

FIG. 4. (Color online) (a)–(c) Experimental transverse (filled black squares) and longitudinal (open black circles) resistivities ρ_T and ρ_L before the onset of nanowire disconnection are plotted in linear scale. ρ_T is fitted with the models discussed in the text. For the sake of clarity, approximately only one data point every 100 has been plotted, but all data points have been used in the fits. The blue line is the result of a calculation according to the FW model in presence of total diffuse scattering ($p = 0$); the dashed red line is the best fit of the experimental data obtained by using the NP model. (a) For sample a, ion fluencies from $\Theta_1 = 7.5 \times 10^{17}$ ions/cm^2 to $\Theta_2 = 15 \times 10^{17}$ ions/cm^2. (b) For sample b, ion fluencies from $\Theta_2 = 15 \times 10^{17}$ ions/cm^2 to $\Theta_3 = 30 \times 10^{17}$ ions/cm^2. (c) For sample c, ion fluencies from $\Theta_3 = 30 \times 10^{17}$ ions/cm^2 to $\Theta_4 = 50 \times 10^{17}$ ions/cm^2.

with a perfect Gaussian height distribution, the corrective factor S providing the total excursion $2B$ of the statistical distribution should thus read as $S = 2B/h = 6/2\sqrt{2} \cong 2.1$.

In Figs. 4(a)–4(c), we plot the transverse (black squares) and longitudinal (open circles) resistivity ρ_T and ρ_L for samples a, b, and c in linear scale and compare them with the models. The data ranges for the analysis were selected in order to exclude the initial thermal transient at low fluences; at high fluences, the range was limited *below* the onset of Au film disconnection, where a different conduction regime dominated by percolation is active. In practice, the latter condition is satisfied when the upper limit of the transverse resistivity is chosen below $\rho_T \approx 90$ Ωnm, where the resistivity ratio ρ_T/ρ_L is around 2 for all samples. As evidenced by the horizontal dashed line in Fig. 3(b), depending on the initial thickness of the Au films, equivalent values of the transverse resistivity (i.e., of the resistivity anisotropy) are obtained for significantly different residual film thicknesses since the amplitude of the ripple corrugation of the sputtered film grows with sputtering time. Given the different initial thickness of samples a, b, c, the data ranges selected for the fits of the resistivity data correspond to three sequential temporal windows, which can be expressed in terms of ion fluences Θ from $\Theta_1 = 7.5 \times 10^{17}$ ions/cm^2 to $\Theta_2 = 15 \times 10^{17}$ ions/cm^2 for sample a [Fig. 4(a)], from $\Theta_2 = 15 \times 10^{17}$ ions/cm^2 to $\Theta_3 = 30 \times 10^{17}$ ions/cm^2 for sample b [Fig. 4(b)], and finally from $\Theta_3 = 30 \times 10^{17}$ ions/cm^2 to $\Theta_4 = 50 \times 10^{17}$ ions/cm^2 for sample c [Fig. 4(c)]. Calculations based on the FW model (red dashed lines) confirm that this mathematical description is not sufficient to interpolate the fast increase of ρ_T even in the case fully diffusive scattering is considered ($p = 0$, i.e. $C \approx 15$ nm). Instead, the best agreement (cyan line) is found using the NP model, which provides an excellent fit of the transverse resistivity measured for the three different samples. The best-fit parameters of the transverse resistivity ρ_T which are obtained from the NP model for the three different samples are here summarized: the bulk resistivity ρ_0 varies in the range 43−46 Ωnm, a reasonable figure for a polycrystalline gold film, taking into account scattering from grain boundaries, which should be compared with $\rho_0 \approx 30$ Ωnm in the case of bulk Au at room temperature. The corrective factor S, which takes into account the long-wavelength modulation of the ripple envelope derived from the fit, is comparable (within 5%) for all the samples around S ≈ 1.7. This figure is thus compatible with the experimentally observed quasi-Gaussian height distribution. The parameter C, proportional to $(1\text{-}p)$, the fraction of electrons which are diffusely scattered at the surface by atomic-scale defects, scales down with increasing ion fluence. The best-fit values for C change from $C \approx 7$ nm ($p \approx 0.5$, i.e., around 50% of the electrons are diffusely scattered) for sample a with initial thickness $d_0 = 80$ nm to $C \approx 3$ nm ($p \approx 0.8$, i.e., around the 20% of electrons are diffusely scattered) for the sample b with initial thickness $d_0 = 150$ nm, and finally for sample c with initial thickness $d_0 = 300$ nm, C is close to 0 (specular reflection condition, $p \approx 1$). The scaling of the parameter C indicates that the small-scale roughness components (surface defects, atomic steps) responsible for diffusive scattering of electrons at the vacuum interface contribute predominantly at lower ion doses to the observed enhancement of transverse resistivity; for higher ion doses, the increase of resistivity is instead dominated by the large-scale roughness components, i.e., thickness fluctuations due to the presence of a ripple pattern. The progressive reduction of electron diffuse scattering (the specularity parameter p progressively decreases to 0) is reasonable since ion bombardment is known to induce local annealing and recrystallization of the metal surface in the hyperthermal transient following ion impact. In this way, the density of atomic steps and defects is reduced on a lateral scale of few nanometers from the ion impact site, compatibly with the spatial distribution of dissipated energy.[18,19] In addition, under the grazing sputtering conditions here employed, the

roughness components are selectively smoothed along the beam direction.[9,10] This leads to an unbalanced distribution of the density of defect sites at the atomic scale (kinks, atomic steps), which decrease along the ion beam projection. The observed decrease of resistivity along the longitudinal direction [bottom open circles in Figs. 4(a)–4(c)] can now be interpreted in light of the former discussion: in this case, the smoothing action of the beam at the small scale is not compensated by the amplification of a large-scale ripple corrugations orthogonal to the electronic motion and a net decreasing trend of ρ_L is observable when the film thickness is progressively reduced.

V. CONCLUSION

In conclusion, benefiting from an original experimental approach, we have been able to disentangle the role of electron scattering at the anisotropically corrugated surface of a nanostructured metal film from the other terms which contribute to electrical resistivity. The results demonstrate that, in the size-effect regime, control of the nanoscale surface morphology of the metal electrode by self-organized ion beam sputtering provides a handle for tailoring the anisotropy of electrical resistivity; in particular, electronic transport parallel to the surface undulations results strongly favored with respect to the orthogonal case well before the corrugated film disconnects into an array of nanowires. The excellent agreement between the experimental trends of transverse resistivity and the Namba-Prater model confirms that the increase of transverse resistivity with ion fluence is determined by the amplification of large-scale ripple undulations. At the same time, the increase of the specularity parameter demonstrates that grazing incidence ion sputtering favors the local smoothing of the small-scale features responsible for diffuse electron scattering. For this reason, the longitudinal resistivity shows a slight but remarkable decrease down to film thicknesses in the 20-nm regime.

ACKNOWLEDGMENT

We acknowledge support by MIUR under Project No. PRIN 2008J858Y7, by CNISM under project Innesco, by MAE under GR bilateral program, by Fondazione CARIGE, and by ENEA under contract MSE.

*Present address: Laboratorio MDM CNR-IMM, Via C. Olivetti 2, Agrate Brianza (MB), I-20864, Italy.
†Present address: Nanobiotech Facility, Istituto Italiano di Tecnologia, via Morego 30, Genova, I-16163, Italy.
‡Corresponding author: buatier@fisica.unige.it

[1] P. Wissmann and H.-U. Finzel, *Electrical Resistivity of Thin Metal Films* (Springer, Berlin, 2007), Vol. 223.
[2] K. Fuchs, Proc. Cambridge Philos. Soc. **34**, 100 (1938).
[3] E. H. Sondheimer, Adv. Phys. **1**, 1 (1952).
[4] S. M. Rossnagel and T. S. Kuan, J. Vac. Sci. Technol. B **22**, 240 (2004).
[5] A. F. Mayadas and M. Shatzkes, Phys. Rev. B **1**, 1382 (1970).
[6] W. G. Ma, H. D. Wang, X. Zhang, and W. Wang, J. Appl. Phys. **108**, 064308 (2010).
[7] W. L. Chan and E. Chason, J. Appl. Phys. **101**, 121301 (2007).
[8] M. Makeev, R. Cuerno, and L. Barabasi, Nucl. Instrum. Methods Phys. Res., Sect. B **197**, 185 (2002).
[9] A. Toma, D. Chiappe, B. Šetina Batič, M. Godec, M. Jenko, and F. Buatier de Mongeot, Phys. Rev. B **78**, 153406 (2008).
[10] A. Toma, B. Šetina Batič, D. Chiappe, C. Boragno, U. Valbusa, M. Godec, M. Jenko, and F. Buatier de Mongeot, J. Appl. Phys. **104**, 104313 (2008).
[11] P. Karmakar and D. Ghose, Surf. Sci. **554**, L101 (2004).
[12] K. Zhang, F. Rotter, M. Uhrmacher, C. Ronning, J. Krauser, and H. Hofsäss, New J. Phys. **9**, 29 (2007).
[13] D. Chiappe, A. Toma, Z. Zhang, C. Boragno, and F. Buatier de Mongeot, Appl. Phys. Lett. **97**, 053102 (2010).
[14] A. Toma, D. Chiappe, C. Boragno, and F. Buatier de Mongeot, Phys. Rev. B **81**, 165436 (2010).
[15] H.-U. Finzel and P. Wissmann, Ann. Phys. (NY) **43**, 5 (1986).
[16] Y. Namba, Jpn. J. Appl. Phys. **9**, 1326 (1970).
[17] W. L. Prater, E. L. Allen, W.-Y. Lee, M. F. Toney, A. Kellock, J. S. Daniels, J. A. Hedstrom, and T. Harrell, J. Appl. Phys. **97**, 093301 (2005).
[18] A. Molle, F. Buatier de Mongeot, A. Molinari, C. Boragno, and U. Valbusa, Phys. Rev. B **73**, 155418 (2006).
[19] C. Busse, H. Hansen, U. Linke, and T. Michely, Phys. Rev. Lett. **85**, 326 (2000).